Magnetic and electrical properties of a heavy-fermion compound $EuRh_2Al_8$

Miao He,[1,2] Xitong Xu,[1,*] Ziyang Wu,[3] Chao Dong,[3] Yonglai Liu,[1,2] Qingyi Hou,[1,2] Shiming Zhou,[4] Yuyan Han,[1] Junfeng Wang,[3] and Zhe Qu[1,2,†]

[1]*Anhui Key Laboratory of Condensed Matter Physics at Extreme Conditions, CAS Key Laboratory of Photovoltaic and Energy Conservation Materials, High Magnetic Field Laboratory of Chinese Academy of Sciences (CHMFL), HFIPS, CAS, Hefei, 230031, China*

[2]*Science Island Branch of Graduate School, University of Science and Technology of China, Hefei 230026, China*

[3]*Wuhan National High Magnetic Field Center and School of Physics, Huazhong University of Science and Technology, Wuhan 430074, China*

[4]*Hefei National Research Center for Physics Sciences at the Microscale, University of Science and Technology of China, Hefei 230026, China*

(Received 15 November 2022; accepted 17 February 2023; published 13 March 2023)

We report the magnetic, thermodynamic, and electrical properties of $EuRh_2Al_8$, a Eu-based heavy fermion member in the RT_2X_8 families with an orthorhombic *Pbam* structure. Magnetization studies reveal multiple phase transitions in the single crystals, including two successive antiferromagnetic transitions at $T_{N1} \sim 12.5$ K and $T_{N2} \sim 8.2$ K. These two transitions are closely related to competing magnetic interactions in the Shastry-Sutherland lattice, which further give rise to another in-plane spin-flop transition at 1/3 of the full magnetization below 5 K when the applied magnetic field is higher than 6 T within the *ab* plane. In addition to these, specific heat measurements in $EuRh_2Al_8$ demonstrate a heavy fermion state with a large Sommerfeld coefficient $\gamma = 393\ \mathrm{mJ \cdot mol^{-1} \cdot K^{-2}}$. Electrical transport measurement shows that its resistivity exhibits a T^2-dependence below T_{N2} and a robust linear T-dependence above T_{N1}, which is also typical of a heavy fermion metal. Our work provides fundamental physical properties of $EuRh_2Al_8$ and promotes understanding of the complex magnetic interactions and unusual spin correlations in the RT_2X_8 families.

DOI: 10.1103/PhysRevMaterials.7.033401

I. INTRODUCTION

Research on rare-earth and transition-metal magnetic intermetallic compounds is at the forefront of condensed matter physics. The interplay between $4f$ and d electrons can trigger various emergent phenomena, including the heavy fermion state [1–8], the Kondo effect [9,10], unconventional superconductivity [11,12], non-Fermi liquid behavior [13,14], and the recently discovered topological states with strong correlations [15–18]. Among these, the heavy fermion materials, characterized by the greatly enhanced effective charge-carrier masses, have been a fertile playground for correlated physics like quantum criticality or quantum phase transitions [19–21].

Recently, a family of RT_2X_8 (R = rare-earth elements, T = transition metals, X = p block elements) ternary intermetallic compounds with over 30 reported members received considerable interests due to the rich electronic and magnetic states [22]. RT_2X_8 compounds were mainly reported to form into the monoclinic (space group $C2/m$) or orthorhombic (*Pbam*) crystal structures. The first is only reported in $CePd_2Al_8$ with Ce-centered $CeAl_{14}$ cages derived from a cuboctahedron, which was found to be a ferromagnetic (FM) Kondo lattice with an antiferromagnetic (AFM) transition at 9.8 K and a FM transition at 8.7 K [23,24]. The other orthorhombic $CaCo_2Al_8$-type structure (Fig. 1) features a face-sharing TX_9 polyhedral network enclosing the R chains along the [001] direction. Interestingly, the R elements also form a set of triangles and squares when viewed along the c direction [Fig. 1(b)], which is found to be topologically equivalent to a Shastry-Sutherland lattice [25]. The rare-earth ions sublattice in this structure can therefore provide magnetic frustrated ground states, which is crucial to realize fractional magnetization plateaus and intertwined quantum fluctuation behaviors [26–29].

Previous investigations revealed exotic physical properties as a result of competing magnetic interactions and unusual spin correlations, including a non-Fermi liquid behavior in the heavy fermion compound $CeCo_2Al_8$ [30], the realization of a one-dimensional Kondo chain in $CeCo_2Ga_8$ [9,31,32], the multiple quantum critical points in $NdFe_2Ga_8$ [33], and other possible heavy fermion superconducting systems [22].

In this work, we synthesized a new Eu-based heavy fermion member $EuRh_2Al_8$, and investigated the magnetic and electrical properties in single crystals. It was found that $EuRh_2Al_8$ undergoes two successive AFM transitions at $T_{N1} \sim 12.5$ K and $T_{N2} \sim 8.2$ K. These two transitions are dominated by the magnetic coupling along the c direction and the in-plane AFM coupling, respectively. With in-plane magnetic field above 6 T, there exists another FM-like spin-flop transition at 1/3 of the full magnetization at even lower temperatures. We also identified heavy fermion behavior with a large Sommerfeld coefficient $\gamma = 393\ \mathrm{mJ \cdot mol^{-1} \cdot K^{-2}}$ in specific heat measurements. Electrical transport measurement reveals that its resistivity shows a crossover from a Fermi-liquid-like behavior below T_{N2} to T-linear behavior above T_{N1}, which is also typical in the heavy fermion members

*xuxitong@hmfl.ac.cn
†zhequ@hmfl.ac.cn

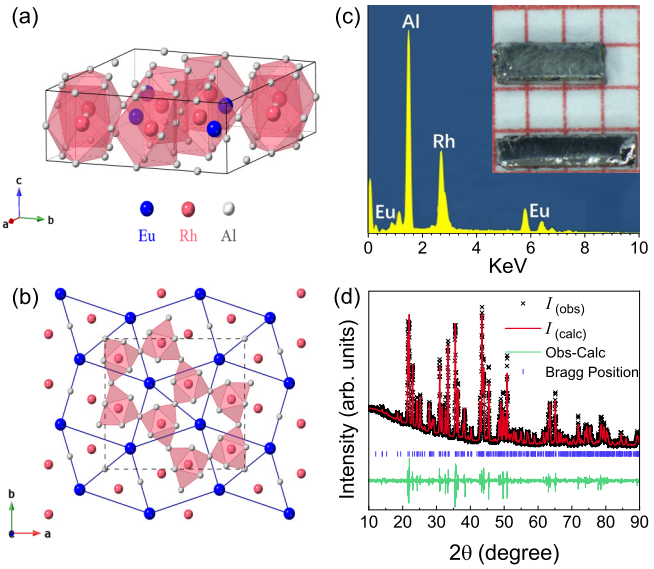

FIG. 1. (a) The unit cell of $EuRh_2Al_8$. (b) Schematic crystal structure of $EuRh_2Al_8$ viewed along the [001] direction, which forms a Shastry-Sutherland lattice. (c) Energy dispersive x-ray spectrum of $EuRh_2Al_8$. The chemical composition is determined to be Eu : Rh : Al = 1 : 2.11 : 7.76, close to the stoichiometric ratio. Inset shows the optical image of as-grown single crystals about 4 mm in length along the *c* axis. (d) Rietveld refinements of the powder XRD pattern for $EuRh_2Al_8$ at 300 K.

like $EuIr_2In_8$ and $PrFe_2Ga_8$ [34,35]. Our results provide fundamental physical properties of $EuRh_2Al_8$ and promote understanding of the complex competing magnetic interactions and unusual spin correlations in the RT_2X_8 families.

II. EXPERIMENTAL TECHNIQUES

Single crystals of $EuRh_2Al_8$ were grown via an Al self-flux method. The starting materials are Eu shots, Rh grains and Al lumps in a molar ratio of 6:8:86, which were put together in an alumina crucible and sealed in a quartz tube with 0.02 MPa argon atmosphere to dilute the Al vapors from attacking the tube walls. The sealed tube was placed in a box furnace, heated to 1050° C over 10 h, held this temperature for 24 h, and subsequently cooled to 900° C at a rate of 2° C/h. After soaking at this temperature for a few hours, the quartz tube was quickly removed from the furnace and centrifuged. Shiny, rod-like single crystals were obtained with a typical dimension of $4 \times 0.5 \times 0.5$ mm^3 as displayed in the inset of Fig. 1(c). The residual tiny Al attached on the surface was removed by mechanical polish and would not influence the experiment results. Single crystals of the nonmagnetic analog $YbCo_2Al_8$ were synthesised by the same method.

The crystal structure of $EuRh_2Al_8$ was determined by both single crystal and powder x-ray diffractions on a SuperNova Rigaku single crystal diffractometer and a Rigaku MiniFlex powder diffractometer, respectively. The structure was solved with the SHELXS structure solution program using DIRECT METHODS and refined with the SHELXL refinement package using LEAST SQUARES minimization [36,37]. Single crystal x-ray diffraction (XRD) data collection and refinement parameters for $EuRh_2Al_8$ are gathered in Tables I, II and III display corresponding atomic coordinates, equivalent isotropic displacement parameters, and anisotropic displacement parameters. Energy dispersive x-ray spectrum (EDX) analysis was performed on an energy dispersive x-ray detector by Oxford Instruments. The magnetic properties were measured with a commercial superconducting quantum

TABLE I. Data collection and refinement parameters for $EuRh_2Al_8$ from single crystal x-ray diffraction.

Chemical formula, Z	$EuRh_2Al_8$, 4
Radiation, λ (Å)	Mo Kα ($\lambda = 0.71073$)
Temperature (K)	293 (2)
Formula weight	622.67
Crystal system	Orthorhombic
Space group	*Pbam*
Unit-cell dimensions	
a (Å)	14.695(11)
b (Å)	12.633(10)
c (Å)	4.114(3)
$\alpha = \beta = \gamma$ (°)	90
Volume (Å^3)	763.63(10)
μ (mm^{-1})	19.183
F(000)	1100.0
Density (g/cm^3)	5.416
Crystal size (mm^3)	$0.19 \times 0.18 \times 0.15$
2θ range for data collection (°)	7.022 to 58.812
Index ranges	$-19 \leqslant h \leqslant 19$, $-11 \leqslant k \leqslant 16$, $-5 \leqslant l \leqslant 3$
Reflections collected	2820
Independent reflections	1048 [$R_{\rm int} = 0.0380$, $R_{\rm sigma} = 0.0383$]
Data/Retraints/Patameters	1048/0/70
Goodness-of-fit on F^2	1.112
Final R indexes [$I \geqslant 2\sigma(I)$]	$R_{\rm obs} = 0.0290$, w$R_{\rm obs} = 0.0647$
Final R indexes [all data]	$R_{\rm all} = 0.0324$, w$R_{\rm all} = 0.0674$
Largest diff. peak/hole (e Å^{-3})	1.68/−2.10

TABLE II. Atomic coordinates and equivalent isotropic displacement parameters for $EuRh_2Al_8$.

Atom	Site	x	y	z	$U_{\rm eq}$ (Å^2)[a]
Eu(1)	4*h*	0.68134(2)	0.34185(3)	1.5	0.00794(15)
Rh(1)	4*h*	0.90445(3)	0.53467(4)	0.5	0.00604(16)
Rh(2)	4*h*	0.59646(2)	0.65242(3)	0.5	0.00481(16)
Al(1)	2*c*	1	0.5	0	0.0085(6)
Al(2)	4*g*	0.87809(15)	0.66281(15)	0	0.0076(4)
Al(3)	4*g*	0.81701(12)	0.45207(17)	0	0.0072(4)
Al(4)	4*h*	0.75238(11)	0.59707(16)	0.5	0.0097(4)
Al(5)	4*g*	0.67482(13)	0.73883(17)	0	0.008(4)
Al(6)	4*g*	0.48942(14)	0.66869(16)	0	0.009(4)
Al(7)	2*b*	0.5	0.5	0.5	0.0099(6)
Al(8)	4*h*	0.54377(14)	0.83984(15)	0.5	0.0108(5)
Al(9)	4*g*	0.63221(13)	0.5245(17)	1	0.008(4)

[a]$U_{\rm eq}$ is defined as one third of the trace of the orthogonalized U_{ij} tensor.

TABLE III. Anisotropic displacement parameters ($Å^2 \times 10^{-3}$) for $EuRh_2Al_8$ at room temperature from single-crystal x-ray diffraction[a].

Atom	U_{11}	U_{22}	U_{33}	U_{12}	U_{13}	U_{23}
Eu(1)	9.4(2)	7.0(2)	7.4(2)	0.7(11)	0	0
Rh(1)	4.3(3)	6.7(2)	7.1(2)	0.46(19)	0	0
Rh(2)	3.5(3)	4.8(3)	6.2(3)	0.19(17)	0	0
Al(1)	6.7(13)	13.4(1	5.4(11)	1.4(12)	0	0
Al(2)	8.9(9)	6.3(11)	7.5(9)	0.4(7)	0	0
Al(3)	6.6(9)	6.6(11)	8.3(8)	−1.4(7)	0	0
Al(4)	4.8(9)	10.7(12)	13.6(9)	0.1(9)	0	0
Al(5)	9.1(9)	7.8(11)	7.1(8)	−2.3(7)	0	0
Al(6)	5.8(9)	9.3(10)	8.8(9)	1.7(8)	0	0
Al(7)	7.8(13)	7.5(14)	14.5(13)	−3.8(11)	0	0
Al(8)	11.2(11)	4.7(12)	16.6(11)	2.3(7)	0	0
Al(9)	7.2(9)	8.0(10)	8.8(8)	0.7(8)	0	0

[a]The anisotropic displacement factor exponent takes the form $-2\pi^2(h^2a^2U_{11} + k^2b^2U_{22} + \ldots + 2Klbc U_{23})$.

interference device (SQUID) magnetometer (MPMS3-7 T, Quantum Design) from 2 K to 300 K along the c axis and ab plane. The isothermal magnetization up to 30 T was measured in a pulsed magnetic field at Wuhan National High Magnetic Field Center. The specific heat and electrical resistivity were performed on the Quantum Design physical property measurement system (PPMS-14 T).

III. RESULTS AND DISCUSSIONS

$EuRh_2Al_8$ belongs to the orthorhombic $CaCo_2Al_8$ structure (space group No. 55, *Pbam*) with lattice parameters $a = 14.695$ Å, $b = 12.633$ Å, and $c = 4.114$ Å, respectively. There are 12 crystallographically unique positions in $EuRh_2Al_8$ structure: one Eu, two Rh, and nine Al atoms. Every Rh atom is surrounded by nine Al atoms, forming a face-sharing $RhAl_9$ polyhedral network that encloses one Eu atom [Fig. 1(a)]. As shown in Fig. 1(b), the rare-earth magnetic ions happen to form a Shastry-Sutherland lattice in a configuration of triangles and squares along the (001) plane [28]. This structure provides AFM couplings between J_1 and J_2 along the diagonals and edges, which is shown to host exotic states like spin liquid, quantum criticality, and exotic magnetization plateaus [26,29,38]. Nevertheless, there is also AFM competition along the c axis as the Eu-Eu distance in this direction (4.114 Å) is much shorter than those between neighboring chains (6.631 and 7.705 Å), which leads to quasi-one-dimensional magnetic behaviors in some 128 members [9,35]. From the results of EDX data in Fig. 1(c), the chemical composition ratio Eu : Rh : Al = 1 : 2.11 : 7.76 is found to be a nearly stoichiometric ratio, indicating that the samples are close to the nominal composition. The refinements of powder XRD patterns are shown in Fig. 1(d), showing good consistency between experiments and calculations (see Supplemental Material [39]). All the results confirm the high quality of our $EuRh_2Al_8$ samples.

We performed magnetization measurements on $EuRh_2Al_8$. Figure 2(a) shows the temperature-dependent magnetic susceptibility χ under an excitation field of 0.1 T for $H//c$ and $H//ab$. The zero-field-cooling and field-cooling cycles are practically identical, suggesting no spin-glass features. Above 20 K, the overall profile of χ is paramagnetic (PM) Curie-Weiss like, as shown in Fig. 2(b). Excellent agreement between the measured data and linear Curie-Weiss law $\chi(T) = C/(T - \theta_p)$ fits is observed in this temperature regime, where C is the Curie constant and θ_p is the Curie-Weiss temperature. This yields $\theta_p = -17.2$ K and an effective moment of $\mu_{\text{eff}} = 8.02\ \mu_B$/Eu for $H//ab$, and $\theta_p = -15.5$ K and $\mu_{\text{eff}} = 7.91\ \mu_B$/Eu for $H//c$. The obtained values of μ_{eff} for both directions are close to the full value of $g\sqrt{S(S+1)}\mu_B = 7.94\ \mu_B$ for the divalent state Eu^{2+} with $S = 7/2$, $L = 0$. The negative θ_p indicates an AFM coupling between Eu^{2+} ions. The anisotropic ratio χ_c/χ_{ab} is close to 1 for these temperatures, suggesting a weak magnetic anisotropy [Fig. 2(b)].

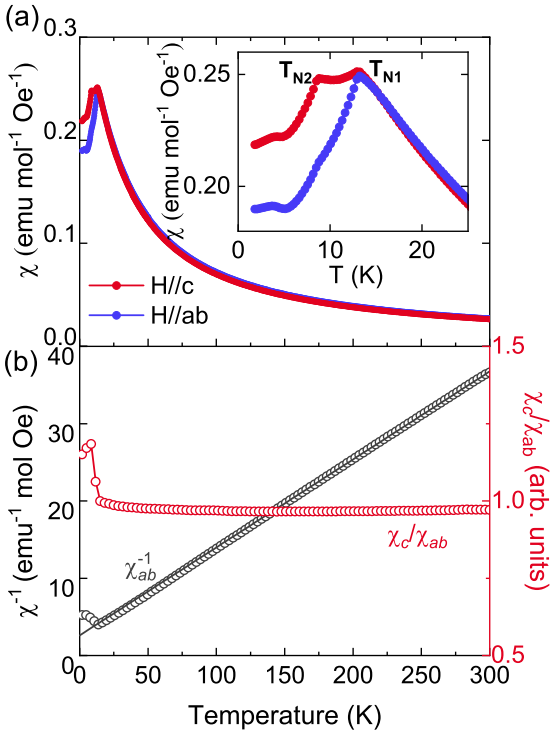

FIG. 2. (a) Temperature dependence of the magnetic susceptibility χ measured under 0.1 T. The inset highlights the 2–25 K regimes, where two successive AFM transitions occur at T_{N1} and T_{N2}. (b) The inverse magnetic susceptibility χ_{ab}^{-1} (left axis) within the ab plane and the anisotropic ratio χ_c/χ_{ab} (right axis). The black line represents the best fit of the Curie-Weiss law at $100 \leqslant T \leqslant 300$ K.

At lower temperatures, there are two obvious downturns in both orientations as shown in Fig. 2(a), inset, indicating two successive AFM transitions in $EuRh_2Al_8$ at $T_{N1} \sim 12.5$ K and $T_{N2} \sim 8.2$ K, respectively. Despite the same structure and electron counts, this T_{N1} is smaller than the AFM onset temperature of the sibling $EuRh_2Ga_8$ (20 K) yet higher than that of $EuRh_2In_8$ (5 K) [40]. To understand the underlying mechanism of these two AFM transitions, we measured the temperature dependence of the magnetic susceptibility at various applied magnetic fields for both the $H//c$ and $H//ab$ directions as shown in Figs. 3(a) and 3(b), respectively. Both T_{N1} and T_{N2} undergo an apparent shift to lower temperatures at

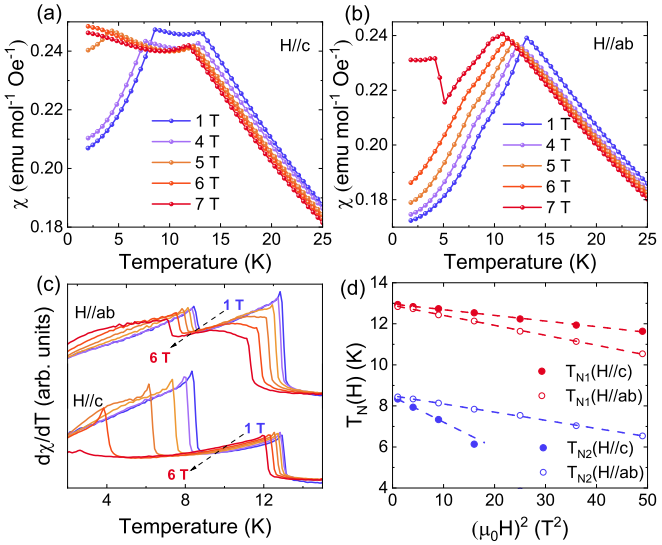

FIG. 3. (a)–(c) Temperature dependence of the magnetic susceptibility χ with $d\chi/dT$ curves at various applied magnetic fields for $H//c$ and $H//ab$. (d) The PM-AFM transition boundaries for T_{N1} and T_{N2} in different directions.

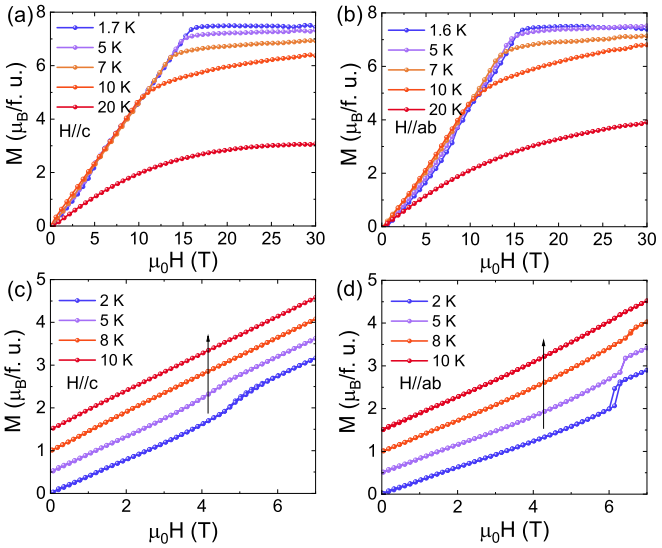

FIG. 4. (a), (b) The isothermal magnetization measured in a high pulsed magnetic field up to 30 T at representative temperatures for $H//c$ and $H//ab$. (c), (d) The isothermal magnetization measured within 0–7 T. Curves are shifted vertically for clarity.

higher fields, although T_{N2} can no longer be identified above 6 T along the c axis. Interestingly, the increased fields cause the T_{N1} curves to shift more rapidly within the ab plane than along the c axis, whereas T_{N2} shifts more swiftly for the c axis field, as shown by the deferential $d\chi/dT$ plots in Fig. 3(c). In a simple uniaxial antiferromagnet with small anisotropy energy, the molecular-field approximation gives a prediction that the paramagnetic-antiferromagnetic (PM-AFM) transition boundaries $T_N(H)$ near the zero-field $T_N(0)$ could be described by the relation [41–43]

$$T_N(0) - T_N(H) = C(\theta)H^2 \propto (1 + 2\cos^2\theta)T_N(0)H^2,$$

where the coefficient C depends on the exchange constants and the angle θ between magnetic field and the preferred axis for the AFM order. For the field along and perpendicular to the preferred axis, $C_{\parallel}$ is three times $C_{\perp}$. Using the peaks in the $d\chi/dT$ plots as the PM-AFM boundaries, we fitted $T_N(H)$ in Fig. 3(d). All the plots show a linear relation with respect to H^2. For T_{N1}, $C_{\perp} = 1.7C_{\parallel}$ and for T_{N2}, $C_{\parallel} = 3.1C_{\perp}$. This indicates that these two transitions are controlled by different magnetic couplings, where the first features the intrachain $4f$ interaction more and the second is primarily affected by the in-plane Shastry-Sutherland lattice arrangement.

The molecular-field model also predicts a first-order spin-flop transition when the field is parallel to the preferred axis. As shown in Figs. 3(a) and 3(b), when the applied magnetic field is higher than 6 T, there exists another FM-like magnetic transition as indicated by the downturn of χ for $H//c$ and the plateau for $H//ab$ below 5 K. This is also verified by the isothermal magnetization measurements where a series of clear hysteresis are found at 6 T between increasing and decreasing field processes within the ab plane as shown in Fig. 4(d). On the other hand, applying external fields along the c axis causes the magnetization to increase relatively smoothly with only slight slope changes. For the magnetic field applied within the ab plane, this flopped spin moment (2.62 μ_B/f.u.) happens to be at 1/3 of the saturated moment of Eu^{2+}, as revealed by pulsed magnetic field measurements in Fig. 4(b). This is reminiscent of the Shastry-Sutherland compounds $SrCu_2(BO_3)_2$ and TbB_4 where multistep quantized magnetization plateaus (including the 1/3 one) were observed [26,44]. $EuRh_2Al_8$ is therefore another interesting example of the Shastry-Sutherland models exhibiting complex magnetic competitions.

Further information on the multiple phase transition in $EuRh_2Al_8$ can be inferred from the specific heat data [$C_p(T)$] as depicted in Fig. 5(a). The two AFM transitions manifest themselves in the sharp, λ-like increases of the specific heat at 12.2 K and 8.2 K under zero field, consistent with the magnetic susceptibility results. With increasing magnetic fields [the top inset of Fig. 5(a)], both of the AFM peaks shift toward lower temperatures, and a third cusp emerges at 5.9 K under external magnetic field 7 T, corresponding to the field induced spin-flop process as seen by magnetization measurements.

The total specific heat contains three parts:

$$C_p = C_{\rm ph} + C_{\rm ele} + C_{\rm mag},$$

where $C_{\rm ph}$, $C_{\rm ele}$, and $C_{\rm mag}$ are the phonon, electronic, and magnetic contributions to specific heat, respectively. At low temperatures, $C_{\rm ph} = \beta T^3$, $C_{\rm ele} = \gamma T$, where β is the constant associated with Debye temperature and γ is the Sommerfeld coefficient that can be interpreted as $C_{\rm ele}$ scaling linearly in temperature. For an estimation of the overall $C_{\rm ph}$, we measured the specific heat of the nonmagnetic analog $YbCo_2Al_8$. Assuming the C_{ph} of $EuRh_2Al_8$ is the same as the nonmagnetic analog $YbCo_2Al_8$ up to a scale factor $\theta_D(T) \propto M_0^{-1/2}V_0^{-1/3}$, where θ_D, M_0, and V_0 are the Debye temperature, the molar mass, and volume, respectively [45,46], we can recalculate the lattice specific heat of $EuRh_2Al_8$ as shown by the red circles in Fig. 5(a). The estimated $C_{\rm ph}$ is well described

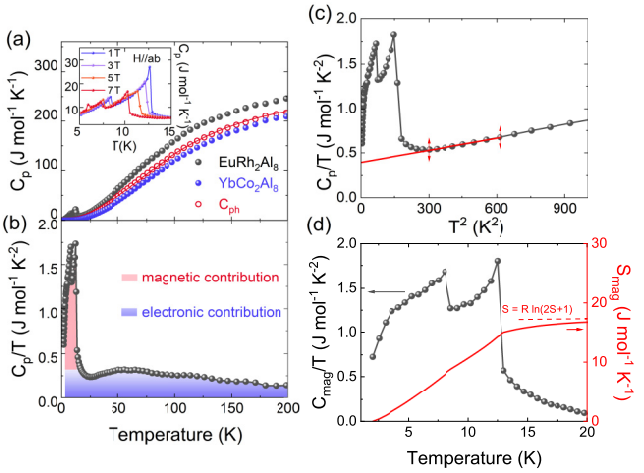

FIG. 5. (a) The zero-field specific heat $C_p(T)$ of $EuRh_2Al_8$ (black circles) and $YbCo_2Al_8$ (blue circles) and the estimated phonon contribution of $EuRh_2Al_8$ (red circles) that is scaled by a factor as explained in the text. The red line represents the best fit of the Debye-Einstein model. The top inset displays the specific heat $C_p(T)$ at different external magnetic fields within the *ab* plane. (b) Temperature dependence of the the magnetic specific heat plus the electronic specific heat. The red and blue shaded areas represent the magnetic and electronic contributions, respectively. (c) The C_p/T versus T^2 plot at low temperatures. The red line is a linear fit to obtain the Sommerfeld coefficient. (d) Temperature dependence of the magnetic specific heat $C_{\rm mag}/T$ (left axis) and the corresponding magnetic entropy $S_{\rm mag}$ (right axis).

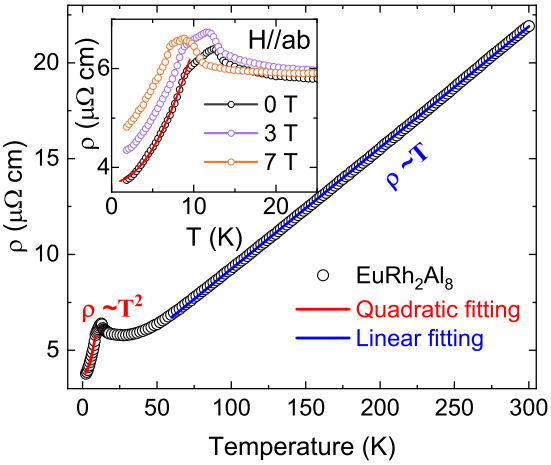

FIG. 6. Temperature dependence of electrical resistivity for $EuRh_2Al_8$ from 2 to 300 K at zero magnetic field. The red and blue parts exhibit the T^2-dependence and linear T-dependence, respectively. Inset is a zoom-in for 2–25 K under different field intensity within *ab* plane.

by the Debye-Einstein model [red line in Fig. 5(a)]

$$C_p = \alpha \cdot 9nR\left(\frac{T}{\theta_D}\right)^3 \int_0^{\theta_D/T} \frac{x^4 e^x}{(e^x-1)^2} dx + (1-\alpha)\cdot 3nR\left(\frac{\theta_E}{T}\right)^2 e^{\theta_E/T}(e^{\theta_E/T}-1)^{-2},$$

yielding Debye and Einstein temperatures: $\theta_D = 470.7\,\mathrm{K}$, $\theta_E = 126.8\,\mathrm{K}$. The low θ_E may be related with local vibration modes in this caged crystal structure. After subtracting the phonon contribution, we obtain the magnetic specific heat plus the electronic specific heat ($C_{\rm mag} + C_{\rm ele}$), as plotted in Fig. 5(b). It can be seen that $(C_{\rm mag} + C_{\rm ele})/T$ is dominated by the magnetic part (red shaded area) at low temperatures, whereas a large portion of electronic contribution (blue shaded area, which also varies with temperature) is seen over the whole temperature range.

To get an accurate $C_{\rm ele}$ at low temperatures, the nonmagnetic part of the specific heat can be well fitted below 30 K by the formula $[(C_{\rm ph} + C_{\rm ele})/T = \gamma + \beta T^2]$ [Fig. 5(c)], yielding $\gamma = 393\,\mathrm{mJ\cdot mol^{-1}\cdot K^{-2}}$ and $\beta = 4.52\times10^{-4}\,\mathrm{J\cdot mol^{-1}\cdot K^{-4}}$. This large Sommerfeld coefficient is also consistent with Fig. 5(b) in the range of $\gamma = 100 \sim 300\,\mathrm{mJ\cdot mol^{-1}\cdot K^{-2}}$. This value is much larger than for a normal metal and is compared to isostructural heavy-fermion RT_2X_8 compounds, for which it varies from 100 to 800 $\mathrm{mJ\cdot mol^{-1}\cdot K^{-2}}$ [22], suggesting that $EuRh_2Al_8$ falls into the category of heavy fermion systems and there exists electron correlation effect contributed from Eu-4f electrons. We also obtained the magnetic specific heat ($C_{\rm mag}$) by subtracting the phonon and electronic contributions from a power-series expansion fits and the magnetic entropy ($S_{\rm mag}$) through the integral of $C_{\rm mag}/T$ versus T, plotted in Fig. 5(d). The magnetic entropy gain below T_{N2} and in between T_{N2} and T_{N1} each constitutes about half of the total spin entropy. The $S_{\rm mag}$ saturates to $16.76\,\mathrm{J\cdot mol^{-1}\cdot K^{-1}}$ above ~20 K, which is very close to the calculated value of the total spin entropy of $S = R\ln(2S+1)$ ($R = 8.314\,\mathrm{J\cdot mol^{-1}\cdot K^{-1}}$, $S = 7/2$ for Eu^{2+}).

We also performed electric characterizations on $EuRh_2Al_8$. Figure 6 shows the electrical resistivity ρ from 2 to 300 K for the current parallel to the *ab* plane. $EuRh_2Al_8$ displays metallic character with a relatively large residual resistivity ratio $\mathrm{RRR} = \rho(300\,\mathrm{K})/\rho(2\,\mathrm{K}) \approx 5.8$. Above T_{N1}, a robust linear resistivity remarkably crosses over most temperature regions with a strange-metal-like feature [47]. Similar T-dependence phenomena were observed for the Eu-caged intermetallic compounds $EuCd_{11}$ [48], $EuTM_2Al_{20}$ (TM = Ti, V) [49], and $EuFe_4Sb_{12}$ [50], which could be attributed to the phonon scattering of interacting electrons in the Eu-4f compounds [48]. Further experimental and theoretical investigations will be needed for fully understanding this unique behavior. Below T_{N2}, the resistivity could be described by the Fermi-liquid-like behavior, $\rho(T) = \rho_0 + AT^2$, with $A = 2.8\times10^{-2}\,\mu\Omega\cdot\mathrm{cm}\cdot\mathrm{K}^{-2}$. This quadratic feature is robust against magnetic field, revealing that electron-electron scattering plays a dominant role at the low-temperature regime [51].

IV. CONCLUSION

In summary, we characterized the magnetic and electrical properties of a new Eu-based heavy fermion member $EuRh_2Al_8$ for the first time. Magnetic measurements reveal that $EuRh_2Al_8$ undergoes two successive AFM transitions at $T_{N1} \sim 12.5$ K and $T_{N2} \sim 8.2$ K. Specifically, T_{N1} is primarily related with the *c*-direction AFM coupling along the shortest Eu^{2+} chains, while the AFM order below T_{N2} appears to have an in-plane preferred axis in the Eu-based

Shastry-Sutherland lattice. This in-plane configuration can be further tuned by an external magnetic field, leading to a spin-flop process at 1/3 of the total magnetic moment. Characteristic heavy fermion behavior is discovered by specific heat measurements with an enhanced Sommerfeld coefficient $\gamma = 393\,\mathrm{mJ}\cdot\mathrm{mol}^{-1}\cdot\mathrm{K}^{-2}$, which offers clear evidence of hybridization between $4f$ electrons and conduction electron states. Electrical transport measurement shows that its resistivity exhibits a T^2-dependence below T_{N2} and a robust linear T-dependence above T_{N1}, indicating a crossover from a Fermi-liquid-like behavior to a strange-metal-like feature. Further theoretic calculations and neutron diffraction experiments will be useful to fully map out detailed formation mechanisms of the magnetic transitions and comprehend the complex spin correlations arising in this interesting compound.

ACKNOWLEDGMENTS

This work was supported by the National Key R & D Program of China Grant No. 2021YFA1600204, National Natural Science Foundation of China Grants No. U1832214, No. U2032213, No. 12104461, and No. 12074135. A portion of this work was supported by the High Magnetic Field Laboratory of Anhui Province. X.X. acknowledges support from the China Postdoctoral Science Foundation Grants No. 2022T150655 and No. 2020M682056, Anhui Postdoctoral Foundation Grant No. 2020B472, Anhui Provincial Natural Science Foundation Grant No. 2108085QA23, Key Lab of Photovoltaic and Energy Conservation Materials Fund, Chinese Academy of Science Grant No. PECL2021ZD003, the HFIPS Director's Fund Grant No. YZJJ2021QN28, and Special Research Assistant Program, Chinese Academy of Sciences.

[1] G. R. Stewart, Rev. Mod. Phys. **56**, 755 (1984).
[2] C. Y. Guo, F. Wu, Z. Z. Wu, M. Smidman, C. Cao, A. Bostwick, C. Jozwiak, E. Rotenberg, Y. Liu, F. Steglich, and H. Q. Yuan, Nat. Commun. **9**, 4622 (2018).
[3] M. D. Bachmann, G. M. Ferguson, F. Theuss, T. Meng, C. Putzke, T. Helm, K. R. Shirer, Y.-S. Li, K. A. Modic, M. Nicklas, M. König, D. Low, S. Ghosh, A. P. Mackenzie, F. Arnold, E. Hassinger, R. D. McDonald, L. E. Winter, E. D. Bauer, F. Ronning *et al.*, and Science **366**, 221 (2019).
[4] Z. F. Weng, M. Smidman, L. Jiao, X. Lu, and H. Q. Yuan, Rep. Prog. Phys. **79**, 094503 (2016).
[5] V.-N. Phan, Phys. Rev. B **101**, 245120 (2020).
[6] Y. Hirose, H. Doto, F. Honda, D. Li, D. Aoki, Y. Haga, and R. Settai, J. Phys.: Condens. Matter **28**, 425601 (2016).
[7] D. Leuenberger, J. A. Sobota, S.-L. Yang, H. Pfau, D.-J. Kim, S.-K. Mo, Z. Fisk, P. S. Kirchmann, and Z.-X. Shen, Phys. Rev. B **97**, 165108 (2018).
[8] Z. Wu, Y. Fang, H. Su, W. Xie, P. Li, Y. Wu, Y. Huang, D. Shen, B. Thiagarajan, J. Adell, C. Cao, H. Yuan, F. Steglich, and Y. Liu, Phys. Rev. Lett. **127**, 067002 (2021).
[9] L. Wang, Z. Fu, J. Sun, M. Liu, W. Yi, C. Yi, Y. Luo, Y. Dai, G. Liu, Y. Matsushita, Y. Dai, G. Liu, Y. Matsushita, K. Yamaura, L. Lu, J.-G. Cheng, Y.-f. Yang, Y. Shi, and J. Luo, npj Quantum Mater. **2**, 36 (2017).
[10] D. Hafner, P. Khanenko, E.-O. Eljaouhari, R. Küchler, J. Banda, N. Bannor, T. Lühmann, J. F. Landaeta, S. Mishra, I. Sheikin, E. Hassinger, S. Khim, C. Geibel, G. Zwicknagl, and M. Brando, Phys. Rev. X **12**, 011023 (2022).
[11] G.-q. Zheng, K. Tanabe, T. Mito, S. Kawasaki, Y. Kitaoka, D. Aoki, Y. Haga, and Y. Onuki, Phys. Rev. Lett. **86**, 4664 (2001).
[12] R. Movshovich, M. Jaime, J. D. Thompson, C. Petrovic, Z. Fisk, P. G. Pagliuso, and J. L. Sarrao, Phys. Rev. Lett. **86**, 5152 (2001).
[13] O. Trovarelli, C. Geibel, S. Mederle, C. Langhammer, F. M. Grosche, P. Gegenwart, M. Lang, G. Sparn, and F. Steglich, Phys. Rev. Lett. **85**, 626 (2000).
[14] G. R. Stewart, Rev. Mod. Phys. **73**, 797 (2001).
[15] J.-X. Yin, W. Ma, T. A. Cochran, X. Xu, S. S. Zhang, H.-J. Tien, N. Shumiya, G. Cheng, K. Jiang, B. Lian, Z. Song, G. Chang, I. Belopolski, D. Multer, M. Litskevich, Z.-J. Cheng, X. P. Yang, B. Swidler, H. Zhou, H. Lin *et al.*, and Nature (London) **583**, 533 (2020).
[16] W. Ma, X. Xu, J.-X. Yin, H. Yang, H. Zhou, Z.-J. Cheng, Y. Huang, Z. Qu, F. Wang, M. Z. Hasan, and S. Jia, Phys. Rev. Lett. **126**, 246602 (2021).
[17] Y. Xu, L. Das, J. Z. Ma, C. J. Yi, S. M. Nie, Y. G. Shi, A. Tiwari, S. S. Tsirkin, T. Neupert, M. Medarde, M. Shi, J. Chang, and T. Shang, Phys. Rev. Lett. **126**, 076602 (2021).
[18] X. Xu, J.-X. Yin, W. Ma, H.-J. Tien, X.-B. Qiang, P. V. S. Reddy, H. Zhou, J. Shen, H.-Z. Lu, T.-R. Chang, Z. Qu, and S. Jia, Nat. Commun. **13**, 1197 (2022).
[19] T. Paschen, S. Lühmann, S. Wirth, P. Gegenwart, O. Trovarelli, C. Geibel, F. Steglich, P. Coleman, and Q. Si, Nature (London) **432**, 881 (2004).
[20] P. Gegenwart, Q. Si, and F. Steglich, Nat. Phys. **4**, 186 (2008).
[21] Q. Si and F. Steglich, Science **329**, 1161 (2010).
[22] M. O. Ogunbunmi, Prog. Solid State Chem. **58**, 100275 (2020).
[23] A. Tursina, E. Khamitcaeva, D. Gnida, and D. Kaczorowski, J. Alloys Compd. **731**, 229 (2018).
[24] L. Wang, C. Wang, Z. Liu, J. Cheng, S. Miao, Y. Song, Y. Shi, and Y.-f. Yang, Phys. Rev. B **100**, 085122 (2019).
[25] Y. I. Dublenych, Phys. Rev. Lett. **109**, 167202 (2012).
[26] S. Yoshii, T. Yamamoto, M. Hagiwara, S. Michimura, A. Shigekawa, F. Iga, T. Takabatake, and K. Kindo, Phys. Rev. Lett. **101**, 087202 (2008).
[27] K. Siemensmeyer, E. Wulf, H.-J. Mikeska, K. Flachbart, S. Gabáni, S. Mat'aš, P. Priputen, A. Efdokimova, and N. Shitsevalova, Phys. Rev. Lett. **101**, 177201 (2008).
[28] M. Ogunbunmi and A. Strydom, Mat. Today Phys. **21**, 100552 (2021).
[29] J. Y. Lee, Y.-Z. You, S. Sachdev, and A. Vishwanath, Phys. Rev. X **9**, 041037 (2019).
[30] S. Ghosh and A. Strydom, Acta Phys. Pol. A **121**, 1082 (2012).
[31] K. Cheng, L. Wang, Y. Xu, F. Yang, H. Zhu, J. Ke, X. Lu, Z. Xia, J. Wang, Y. Shi, Y. Yang, and Y. Luo, Phys. Rev. Mater. **3**, 021402(R) (2019).
[32] A. Bhattacharyya, D. T. Adroja, J. S. Lord, L. Wang, Y. Shi, K. Panda, H. Luo, and A. M. Strydom, Phys. Rev. B **101**, 214437 (2020).

[33] C. Wang, X. Wang, L. Wang, M. Yang, Y. Song, Z. Mi, G. Li, Y. Shi, S. Li, and Y.-f. Yang, Phys. Rev. B **103**, 035107 (2021).
[34] N. P. Calta, S. L. Bud'ko, A. P. Rodriguez, F. Han, D. Y. Chung, and M. G. Kanatzidis, Inorg. Chem. **55**, 3128 (2016).
[35] C. Wang, X. Wang, K. Jia, L. Wang, D. Yan, H. L. Feng, S. Li, and Y. Shi, J. Phys.: Condens. Matter **34**, 165601 (2022).
[36] L. J. Bourhis, O. V. Dolomanov, R. J. Gildea, J. A. K. Howard, and H. Puschmann, Acta Cryst. Found Adv. **71**, 59 (2015).
[37] G. M. Sheldrick, Acta Cryst. Found Adv. **71**, 3 (2015).
[38] M. S. Kim and M. C. Aronson, Phys. Rev. Lett. **110**, 017201 (2013).
[39] See Supplemental Material at http://link.aps.org/supplemental/10.1103/PhysRevMaterials.7.033401 for details of the refined crystal structure of $EuRh_2Al_8$.
[40] V. Fritsch, S. Bobev, N. O. Moreno, Z. Fisk, J. D. Thompson, and J. L. Sarrao, Phys. Rev. B **70**, 052410 (2004).
[41] Y. Shapira, Phys. Rev. B **2**, 2725 (1970).
[42] Y. Shapira, S. Foner, and A. Misetich, Phys. Rev. Lett. **23**, 98 (1969).
[43] Y. Shapira and S. Foner, Phys. Rev. B **1**, 3083 (1970).
[44] T. Momoi and K. Totsuka, Phys. Rev. B **62**, 15067 (2000).
[45] E. S. R. Gopal, *Specific Heats at Low Temperatures* (Plenum, New York, 1966).
[46] S. Nakatsuji, Y. Nambu, H. Tonomura, O. Sakai, S. Jonas, C. Broholm, H. Tsunetsugu, Y. Qiu, and Y. Maeno, Science **309**, 1697 (2005).
[47] B. Shen, Y. Zhang, Y. Komijani, M. Nicklas, R. Borth, A. Wang, Y. Chen, Z. Nie, R. Li, X. Lu, H. Lee, M. Smidman, F. Steglich, P. Coleman, and H. Yuan, Nature (London) **579**, 51 (2020).
[48] A. Nakamura, Y. Hiranaka, T. Uejo, T. Takeuchi, F. Honda, H. Harima, K. Matsubayashi, Y. Uwatoko, M. Hedo, T. Nakama, and Y. Ōnuki, J. Phys. Soc. Jpn. **83**, 074714 (2014).
[49] K. R. Kumar, H. S. Nair, R. Christian, A. Thamizhavel, and A. M. Strydom, J. Phys.: Condens. Matter **28**, 436002 (2016).
[50] B. C. Sales, R. Jin, D. Mandrus, and P. Khalifah, Phys. Rev. B **73**, 224435 (2006).
[51] J. Paglione, M. A. Tanatar, D. G. Hawthorn, E. Boaknin, R. W. Hill, F. Ronning, M. Sutherland, L. Taillefer, C. Petrovic, and P. C. Canfield, Phys. Rev. Lett. **91**, 246405 (2003).